

# Profiling the Eddy Current Losses Variations of High-Speed Permanent Magnet Machines in Plug-in Hybrid Electric Vehicles

Zhen Huang, Mi Tang, Dmitry Golovanov, Tao Yang, Scott Herring, Pericle Zanchetta, Christopher Gerada

**Abstract** – High-speed permanent magnet (PM) machines have been recognized as a popular choice for plug-in hybrid electric vehicles (PHEVs). Although high-speed operation can enhance the machine power density, more rotor eddy current losses can be expected. Those losses dominantly result from the current harmonics that may vary during the vehicle driving cycles. Therefore, it is crucial to profile the eddy current losses variations, thus identifying the worst case. To achieve this objective, a new indicator, namely the frequency-weighted harmonics distortion (FWTH), is defined correlating with eddy current losses in this paper. Profiling eddy current losses variations by FWTH relieves the computational burden seen in the finite element analysis (FEA) as its derivation simply governs all the current harmonics. Various machine and converter operation conditions are covered in the study. The strong correlations between the addressed FWTH factor and the eddy current losses have been validated from the FEA, and then the experimental results on a 110krpm, 35kW PM machine served in PHEVs. The effectiveness of using FWTH to profile the eddy current losses variations during driving cycles has been proven, where the worst eddy current case has been identified for the tested machine.

**Index terms:** *Current harmonics, eddy current losses, high-speed machine, plug-in hybrid electric vehicle, pulse width modulation.*

## I. INTRODUCTION

With ever-increasing demands on emission reduction and fuel-saving, electric vehicles are perceived as the most promising application that can gradually replace traditional fossil fuel vehicles [1-3]. Among all kinds of electric vehicles, plug-in hybrid electric vehicles (PHEVs) stand out as they combine conventional fossil fuel-based propulsion and electric propulsion with the capability of onboard charging [4-6]. In contrast, battery electric vehicles (BEVs) solely rely on the electrified propulsion, but they suffer from a limited driving range and long recharge time [1, 7, 8].

One of the most popular powertrain architectures in PHEVs is the series hybrid [7], as shown in Fig. 1. There are two electric machines (*A* and *B*) in Fig. 1, while the entire mechanical transmission in the traditional vehicle is now removed. Machine *A* coupled to the engine is not mechanically connected to the driving wheels. Thus, the engine is isolated from the vehicle driving cycles, allowing it consistently to operate at its most efficient speed [5]. Since the batteries perform the primary propulsion in PHEVs, the engine can be chosen as a microturbine. Machine *A* in Fig. 1 initially works as a starter accelerating the microturbine. Then, it operates as a generator maintaining the speed of the microturbine while the output power will charge the battery packs when needed.

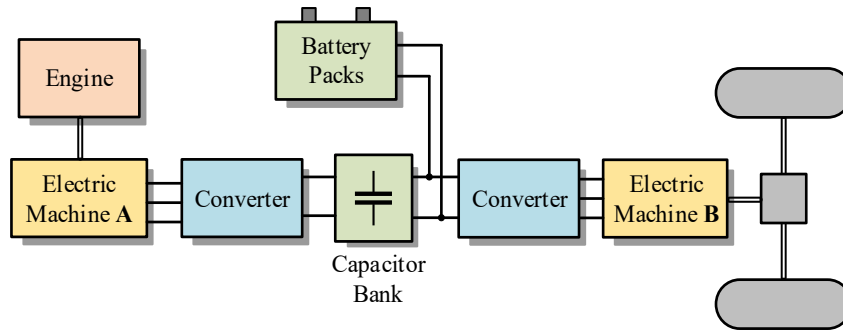


Fig. 1. The architecture of a series-hybrid powertrain adopted in PHEV.

To enhance the power density and efficiency, high-speed permanent magnet (PM) machines are typically adopted in PHEVs [7, 9]. Within the limited space of PHEVs, the electric machines are normally placed close to the engine, where the ambient temperatures can be over 200°C [10]. Such temperature poses a severe threat to the performance of PM material, a part of rotors, due to its low tolerance for the high temperature [4]. On the other side, the rotor cooling can be challenging as the rotors are moving parts, which cannot be well cooled apart from the limited heat transfer through the airgap [11]. Under this case, the rotor losses for electric machines in PHEVs should be well examined.

Rotor losses are mainly attributed to the eddy current losses of the PM and the shaft, which are defined by the spatial harmonics and the time harmonics [12, 13]. The spatial harmonics are determined by the machine design, but the time harmonics may vary according to the vehicle operation. For instance, machine speeds or loads can alter the time harmonics, resulting in varying eddy current losses. On the other side, the battery voltage that feeds onto the converter is not constant depending on the battery state-of-charge (SoC). This aspect can also affect the time harmonics. Therefore, it is crucial of identifying the operation case with the worst eddy current losses.

The time harmonics are associated with implementing pulse width modulation (PWM) techniques [11, 14-17]. With larger speeds, the impact of time harmonics on the eddy current losses aggravates [12, 13, 18]. Further, due

to the physical limitation of solid-state switching devices and the switching losses considerations, the switching frequency cannot be very high [19, 20]. This results in a relatively low sample ratio (the sampling frequency over the fundamental frequency), which essentially degrades the converter output quality by introducing additional harmonics [21]. References [15, 17] reported that the eddy current losses caused by harmonics are related to their amplitudes and frequencies, but the relationship has not been formulated.

To quantify the eddy current losses in high-speed machines caused by the time harmonics, 3D finite element analysis (FEA) is normally required, but it is considerably time-consuming [14]. Researchers in [11, 17] addressed several effective and fast analytical methods. However, the time harmonics distribution is significantly affected by the machine and converter operation conditions, which have not been adequately investigated in the previous works [15, 17]. Some hybrid methods of combining analytical methods with 2D FEA approaches were reported in [14, 16]. Even though those methods can maintain a rather excellent accuracy as using 3D FEA, eddy current losses under the different machine and converter operation conditions still need to be swept by running 2D FEA simulations.

Instead of computing the eddy current losses, a new approach of defining an indicator correlating with the eddy current losses is proposed in this paper. This indicator, namely frequency-weighted total harmonics (FWTH), is simply calculated by governing all the time harmonics, similar to the derivation of total harmonics distortion (THD). Using FWTHs can quickly profile the eddy current losses variations during the vehicle driving cycles. This method will not need for solving any more analytical equations or running FEA simulations.

To access the correlation relationship between the proposed FWTH factor and the eddy current losses, the Pearson correlation coefficient is adopted. As a comparison, the correlation coefficient between the THD and the eddy current losses are also computed. After sweeping the machine and converter operation conditions, FWTH has been proven to be linearly related to the eddy current losses. Therefore, the FWTH can be perceived as a reliable eddy current losses indicator. The linear correlations between the FWTH and the eddy current losses have been validated through simulated and experimental outcomes on a commercial 35kW, 110krpm PM machine designed by Delta Motorsport served in PHEVs.

## II. EDDY CURRENT LOSSES IN ROTORS

### A. Principle of Eddy Current Losses

The general formulation of PM and shaft eddy current loss problem leads to diffusion equation expressed via magnetic vector potential  $A$ , as described in (1). And the corresponding eddy current  $J$  induced in PM and shaft domain can be calculated as (2) [22].

$$\nabla^2 A = -\mu_0 \left( \sigma \frac{\partial A}{\partial t} - \nabla \times M \right) \quad (1)$$

$$J = \sigma \left( -\frac{\partial A}{\partial t} + v \times (\nabla \times A) \right) \quad (2)$$

Here  $\sigma$  is the PM and the shaft material conductivity,  $M$  is the magnetization of PM ( $M = 0$  for the shaft domain),  $v$  is the rotor speed. Various methods (analytical and finite elements) exist to find an exact solution of these equations in 2D or 3D formulation for further eddy current loss evaluation. However, for a general understanding of trends and correlations of eddy current losses for high-speed or high-frequency electric machines, they can be approximated by the eddy current component of Steinmetz equation, as expressed in (3) [23, 24].

$$P = P_{sp} \sum B_n^2 f_n^2 \quad (3)$$

Here  $P_{sp}$  is the specific loss of laminated material,  $B_n$  is the magnitude of the external flux density of  $n^{\text{th}}$  harmonic,  $f_n$  is the  $n^{\text{th}}$  harmonic frequency.

For the ideal current waveform, the eddy current losses are mainly associated with spatial harmonics related to winding layout and slotting effect that introduces magnetic field distortion in the airgap with the corresponding time harmonics. However, if the machine is powered from a converter, then the impact of converter switching frequency to the eddy current loss becomes dominant and should be considered. The high order current harmonics, in this case, will lead to the cumulative eddy current loss effect as it leads from (3), and they need to be summarized.

### B. Time Harmonics Introduced by PWM

Fig. 2 shows a typical motor drive system comprising of a two-level converter and a machine. Depending on the control purposes, the demanded voltage  $V_{ref}$  from the machine is determined and then send this reference value into the modulator implementing the PWM. Based on the DC-link voltage  $V_{dc}$  and  $V_{ref}$ , the modulator will generate

the gate signals sending to the semiconductor switches in Fig. 2. Accordingly, they are switched at a relatively high switching frequency  $f_{sw}$  for assigned duty cycles, achieving a desired low-frequency  $f_m$ , i.e., fundamental-frequency output in an average sense. This average nature indicates that there is an inevitable error between the instantaneously applied voltage vector and the reference vector. Those voltage errors lead to the output current harmonics, as shown in Fig. 2 when fed on a machine.

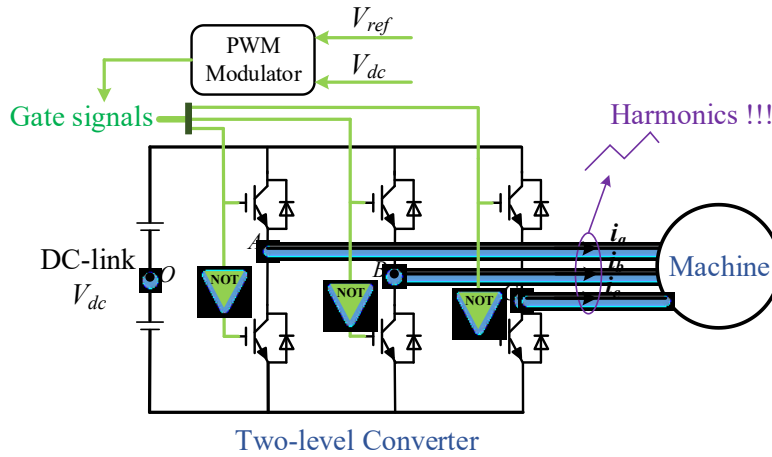


Fig. 2. A typical motor drive system.

After implementing the PWM technique, a typical spectrum of the converter output current harmonics is shown in Fig. 3 [25]. It can be seen that the harmonics are surrounding the multiple times of the switching frequency, i.e.,  $f_{sw}$ ,  $2f_{sw}$ , and  $3f_{sw}$  in Fig. 3. Those harmonics are called sideband harmonics. For instance, the harmonics at  $2f_{sw} \pm f_m$  and  $2f_{sw} \pm 2f_m$  in Fig. 3 are the sideband harmonics of 2<sup>nd</sup> switching frequency, i.e.,  $2f_{sw}$ .

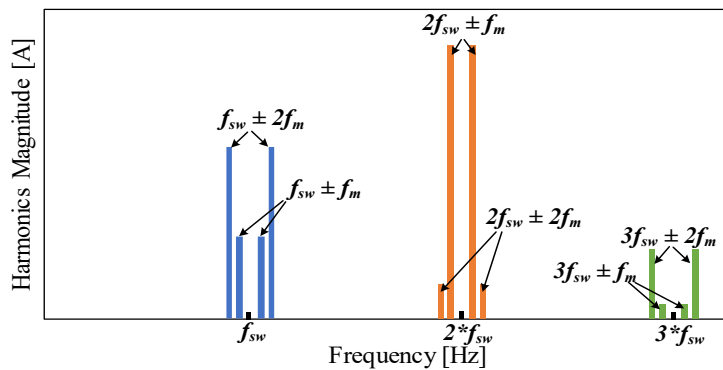


Fig. 3. Current harmonics spectrum after implementing PWM techniques.

### III. PROPOSED EDDY CURRENT LOSSES INDICATOR

Due to the nature of PWM technique, the modulation process inevitably introduces undesirable harmonics into the converter output. To evaluate its quality, the output current THD is usually adopted [1]. It is a very general metric, whereas no specific factor refers to the eddy current losses. In this section, the definition of THD will be briefly described, and then a new indicator correlating with the eddy current losses will be detailed.

#### A. Total Harmonics Distortion

The expression of THD is given in (4),

$$THD = \sqrt{\sum_{n=2}^{\infty} I_{n,rms}^2} / I_{1,rms} \quad (4)$$

Where  $I_{n,rms}$  represents the RMS value of current harmonics at  $n^{th}$  order, and  $I_{1,rms}$  is the RMS value of the fundamental current.

Equation (4) shows that THD derivation directly sums up all the considered current harmonics. However, as revealed in (4), the harmonics at higher orders tend to result in greater eddy current losses. This implies that a lower THD figure maybe not guarantee lower eddy current losses.

#### B. Frequency-Weighted Total Harmonics

A new indicator FWTH defined in (5) is proposed. Instead of simply summing up all current harmonics as seen in THD, FWTH weights the higher portion of the frequency spectra more heavily (i.e., proportional with frequency), accurately portraying the expected, resulting eddy current losses as seen in (3).

$$FWTH = \sum_{n=2}^{\infty} (f_n * I_{n,rms})^2 \quad (5)$$

Assuming the load can be simplified as its total leakage inductance  $L$  with relatively small but non-trivial resistance, and then we can obtain,

$$I_{n,rms} = \frac{V_{n,rms}}{\omega_n L} \quad (6)$$

Where  $V_{n,rms}$  represents the RMS value of voltage harmonics at  $n^{th}$  order, and  $\omega_n$  stands for the angular frequency of harmonics at  $n^{th}$  order.

Substituting  $I_{n,rms}$  from (6) into (5), and we can derive,

$$FWTH = \sum_{n=2}^{\infty} \left( f_n * \frac{V_{n,rms}}{\omega_n L} \right)^2 = \frac{1}{2\pi L} \sum_{n=2}^{\infty} (V_{n,rms})^2 \quad (7)$$

As the RMS value of voltage harmonics can be calculated by subtracting the RMS of the fundamental voltage  $V_1$  from the whole voltage  $V_{rms}$ ,

$$V_{n,rms}^2 = V_{rms}^2 - V_1^2 \quad (8)$$

Substituting (8) into (7),

$$FWTH = \frac{1}{2\pi L} (V_{rms}^2 - V_1^2) \quad (9)$$

From (9), it indicates that FWTH is determined by the  $V_1$  and the  $V_{rms}$ . With different machine speeds and battery voltages, those two numbers may change. However, the machine load condition seems to be irrelevant with the FWTH factor. In the following sections, these initial claims will be examined.

#### IV. EDDY CURRENT LOSSES DERIVATION

This section will investigate the eddy current losses with different machine and converter operation conditions using co-simulation. It feeds the currents with the time harmonics from the switching model for the FEA. Such co-simulation can consider the eddy current losses due to the influence of time harmonics. Besides, the correlation relationship between the eddy current losses and the FWTH will be assessed.

##### A. Machine Preliminary Study

In this paper, a commercial 35kW, 110krpm PM machine designed by Delta Motorsport served in PHEVs is taken for the case study. Its parameters are listed in TABLE I.

TABLE I THE LIST OF MACHINE PARAMETERS FOR ROTOR LOSSES INVESTIGATION

Parameters	Value	Parameters	Value
Number of poles/slots	2/12	Magnetic gap	3.2mm
Number of phases	3	Axial segmentation	1.9mm
Rated speed	110,000rpm	PM material name	N42EH
Rated torque	3.2Nm	PM resistivity	1.8e-06Ω·m
Rated power	35kW	PM residual induction	1.2T

Rotor axial length	65.4mm	Shaft material resistivity	$5.7e-7 \Omega \cdot m$
PMs outer diameter	31.6mm	Nominal phase current	145A (peak)
Shaft outer diameter	13.6mm	Stator outer diameter	100.2mm

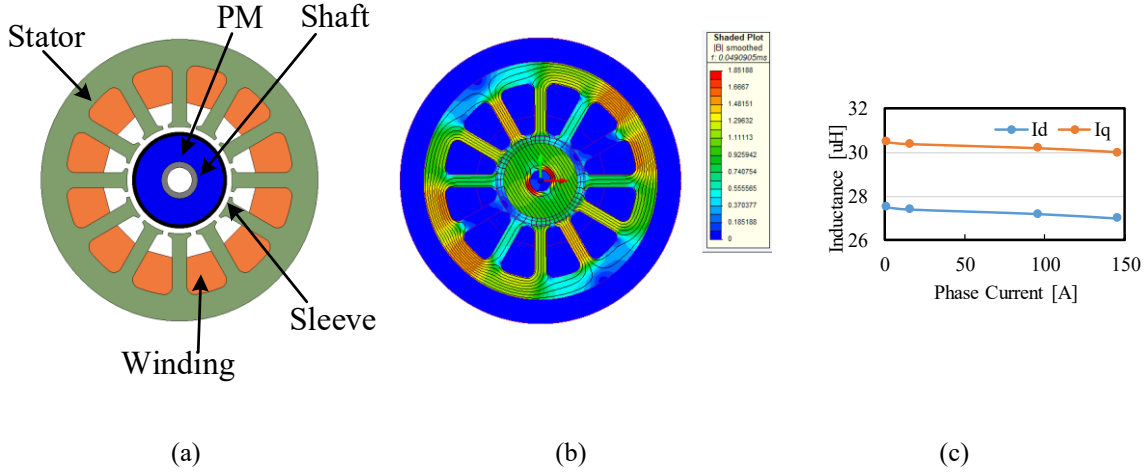


Fig. 4. Machine preliminary study a) geometry; b) flux density distribution; c)  $dq$  inductances at different phase currents.

Fig. 4a shows the geometry of the selected machine. It has three-phase distributed winding placed in 12 semi-closed slots, a two-pole rotor with segmented neodymium PMs, a carbon fibre sleeve, and a hollow magnetic shaft. To conduct a preliminary study, three-phase sinusoidal currents are injected, and the magnetic flux line distribution is shown in Fig. 4b. The back EMF (electromagnetic force) characteristics and the phase inductance matrix table can be derived. This matrix table contains the phase self-inductance and phase-to-phase mutual inductance at different rotor position angles. To involve the saturation effect on the inductance variations, the inductance matrixes at different current levels are obtained. After transforming the inductance matrixes table from  $abc$  frame into  $dq$  frame, the  $d$ -axis inductance  $I_d$  and  $q$ -axis inductance  $I_q$  versus different levels of phase current can be generated, as shown in Fig. 4c.

### B. Co-simulation

A switching model of the motor drive system, as shown in Fig. 2, is built in PLECS environment. The inductance information shown in Fig. 4c and the machine parameters listed in TABLE I can be input into the simulation. Then, the phase currents with time harmonics now can be generated. To evaluate PM eddy current loss at different rotating speeds, a 3D transient FEA was carried out for one PM segment. The 3D simulation was performed for a quarter of the electrical period with 300 steps to save computational time. Due to the PMs segmentation, the contribution of the 1<sup>st</sup> harmonic to the total loss is not significant and can be neglected. Fig. 5 shows the 3D mesh

diagram, where the maximum mesh element size applied for PM segments is 0.75 mm. The average computational time for the presented 3D model is 27 hours by using the computer with the following PC hardware: Intel Xeon CPU E5-1620 v3 at 3.5 GHz, 32-GB RAM.

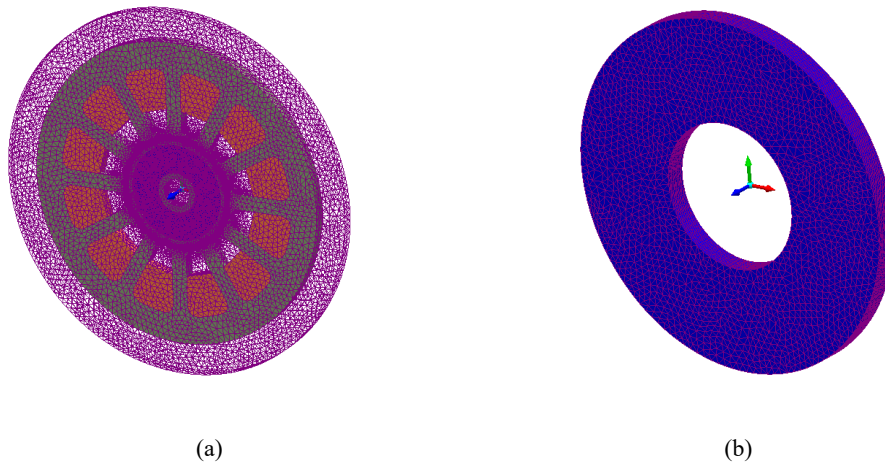


Fig. 5. 3D mesh diagrams of (a) the full PM model; (b) one PM segment.

For the shaft loss estimation, the simulation was carried out in 2D FEA for one electrical period. Neglecting the 3D effects is a typical assumption widely applicable for the models whose axial length is greater than its diameter [14, 26]. As shown in TABLE I, the shaft axial length and diameter are 65.4 mm and 13.6mm, respectively. For the tested shaft, the dominant component of the eddy-current is aligned along the shaft, and the eddy current field in the shaft is predominantly 2D plane-parallel [26].

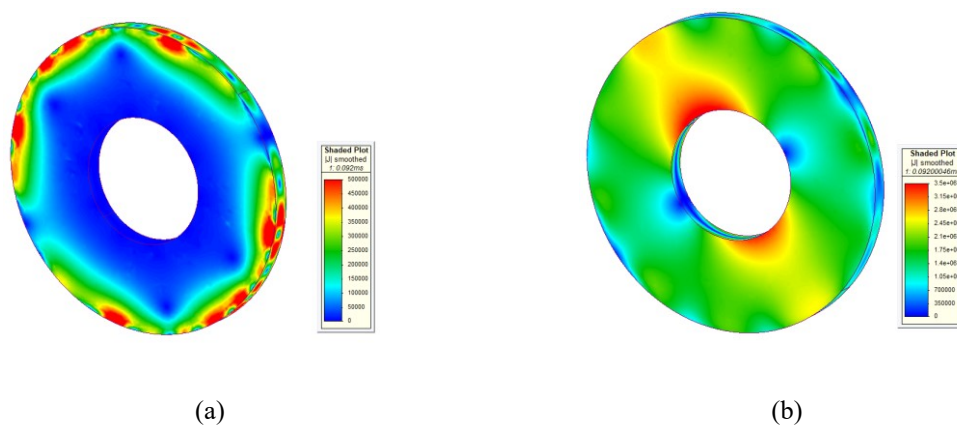


Fig. 6. Eddy currents induced in one PM segment feeding with (a) an ideal sinusoidal current and (b) the currents with time harmonics.

A comparison of instantaneous eddy current distribution in the PMs feeding with ideal sinusoidal three-phase currents and the currents with time harmonics is presented in Fig. 6. The current distributions in Fig. 6a are more

irregular compared to the ones in Fig. 6b. This phenomenon is due to the slotting effect of the non-sinusoidal flux density distribution in the air gap as the machine was designed with semi-closed slots, as shown in Fig. 4a. It can be seen that for the sinusoidal current waveform in Fig. 6a, the amplitude of induced eddy current is significantly lower than for the currents with time harmonics in Fig. 6b. The corresponding PM loss is 1.1W in the case of sinusoidal current waveform while it is reaching 66.3W for the distorted currents.

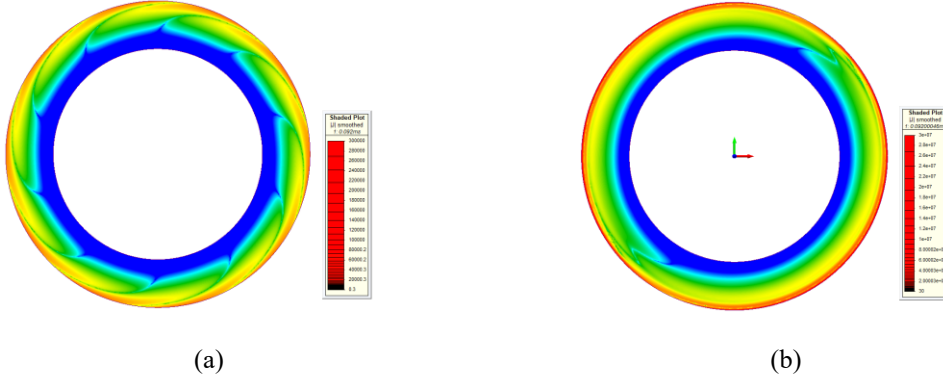


Fig. 7. Eddy currents induced in the shaft feeding with (a) an ideal sinusoidal current and (b) the currents with time harmonics.

The instantaneous eddy current density map for the rotor shaft at the same condition is presented in Fig. 7 on a logarithmic scale. This phenomenon is because the eddy currents are significant on the shaft surface and quickly decrease towards its centre. The estimated eddy current losses for an ideal sinusoidal current are 0.2mW in Fig. 7a, while for the currents with time harmonics, the losses increase significantly up to 69.2W in Fig. 7b.

## V. EDDY CURRENT LOSSES PROFILE

Following the described eddy current losses derivation in the last section, the losses profile of vehicle driving cycles can be studied. As discussed in previous sections, the machine speeds, machine loads, and battery voltages can affect the time harmonics, leading to different eddy current losses. Therefore, in this section, those three influence factors will be investigated in sequence.

## A. Losses versus Machine Speeds

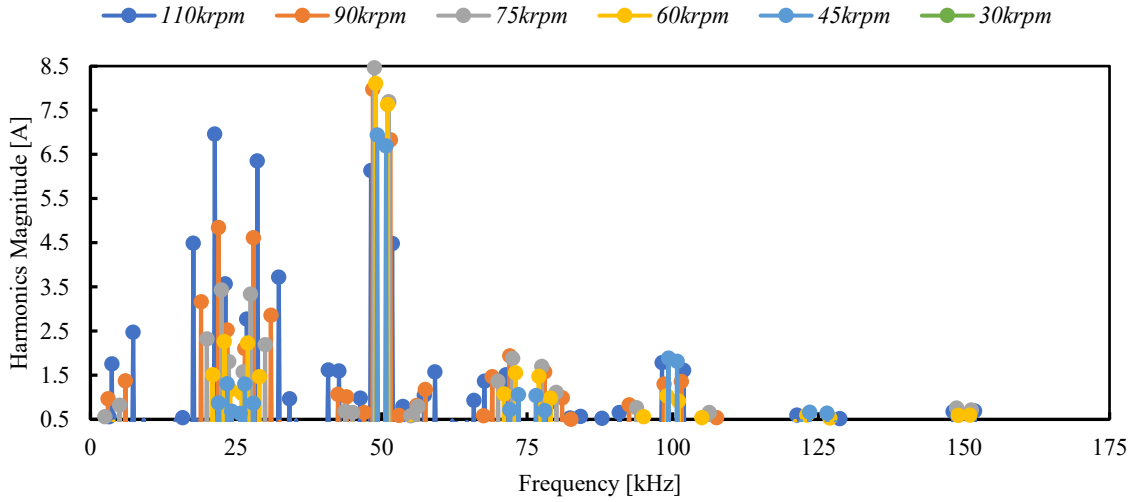


Fig. 8. Magnitudes of current harmonics spectrum with different machine speeds.

Within the series powertrain shown in Fig. 1, the required speed for machines is determined by the engine operation, where the rated speed is 110krpm. To study the eddy current losses versus machine speeds, the DC-link voltage is pre-set at 350V, and the switching frequency is kept at 25kHz. In Fig. 8, the spectrum of converter output currents with speeds ranging from 30krpm to 110krpm is shown. The considered frequency of current harmonics is up to 1MHz, where harmonics with a magnitude lower than 0.25A are omitted for display in Fig. 8. It is clear from Fig. 8 that current harmonics are surrounding at multiple times of the switching frequency  $f_{sw}$ . The primary harmonics are allocated around the 1<sup>st</sup> and 2<sup>nd</sup> of  $f_{sw}$ , 25kHz and 50kHz, in Fig. 8. The magnitude of harmonics is weighted by their corresponding frequency for the same currents, as shown in Fig. 9. The y-axis of Fig. 9 is expressed in the unit of ‘M’, which represents to  $10^6$ . Compared to the magnitudes without frequency-weighted in Fig. 8, the major harmonics now move to the sidebands of 2<sup>nd</sup> and 4<sup>th</sup>  $f_{sw}$ , i.e., 50kHz and 100kHz in Fig. 9.

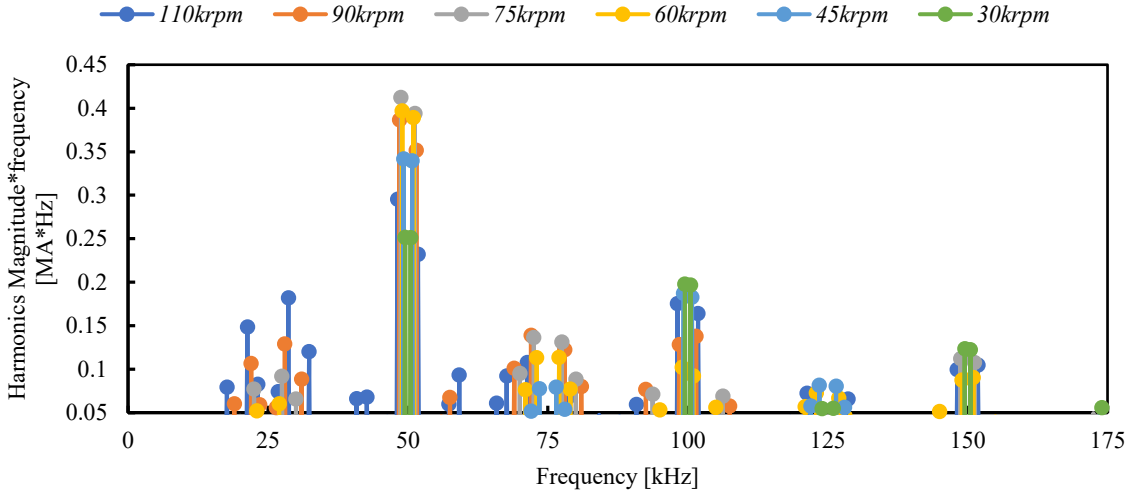


Fig. 9. Frequency-weighted magnitudes of current harmonics spectrum with different machine speeds.

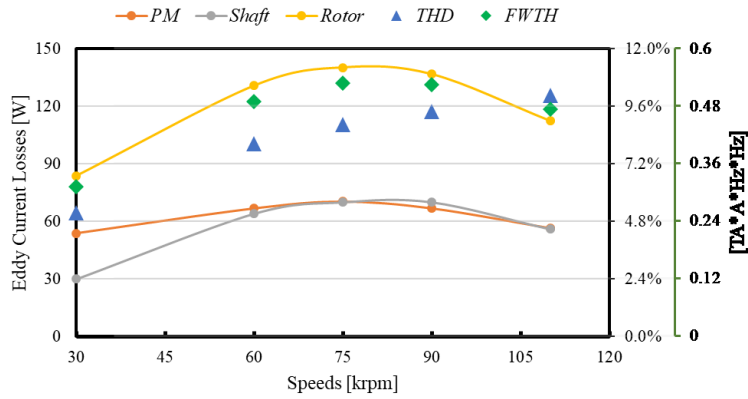


Fig. 10. Rotor losses distribution, THD and FWTH factors versus machine speeds.

Fig. 10 shows the PM losses, the shaft losses and the rotor losses versus different machine speeds obtained from the co-simulation. The current THD calculated by (4) and FWTH calculated by (5) at different speeds are also included in the second and the third vertical axis of Fig. 10, respectively. The FWTH factors are shown in the unit of ‘T’ (tera), which is  $10^{12}$ . It can be seen from Fig. 10 that the current THD is increasing at a higher speed. However, the losses initially climb up with the increasing speeds and then drop at full speed. Thus, Fig. 10 demonstrates that the current THD fails to correlate with the rotor losses. In Fig. 10, it is clearly shown that FWTH with different speeds also has a similar trend as seen in the losses against speeds.

*B. Losses versus Machine Loads*

Within the series powertrain shown in Fig. 1, the required torque for machines depends on the engine operation, where the rated torque is 3.2Nm. To study the sensitivity of eddy current losses against different load torques,

four representative torques are considered for a fixed speed of 75krpm. This speed is chosen because it is identified as the one associated with the most eddy current losses (see Fig. 10). The DC-link voltage and switching frequency are assigned to 350V and 25kHz, respectively.

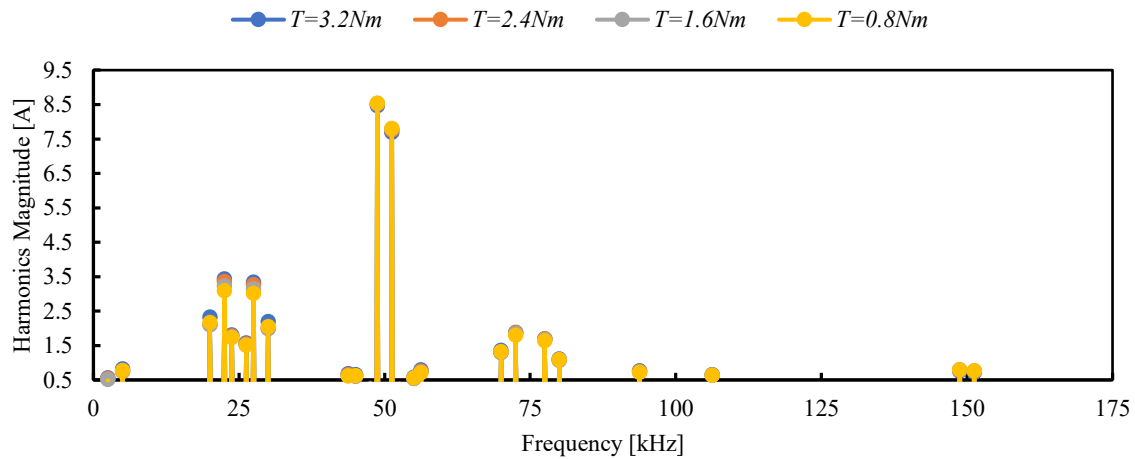


Fig. 11. Magnitudes of current harmonics spectrum with different machine loads.

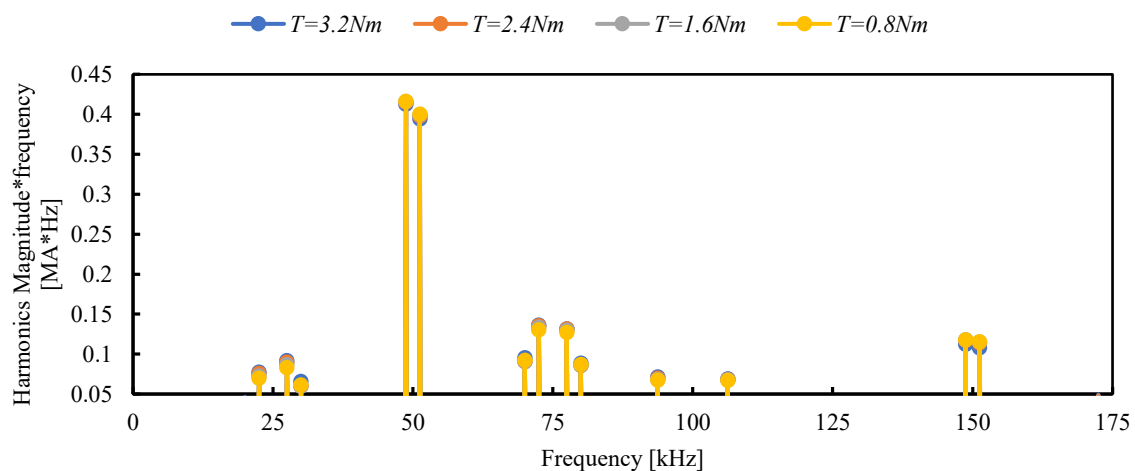


Fig. 12. Frequency-weighted magnitudes of current harmonics spectrum with different machine loads.

Fig. 11 shows the frequency spectrum of output current harmonics with the machine loads changing from 0.8Nm to 3.2Nm. And those harmonic magnitudes are weighted by their frequencies in Fig. 12. It is apparent from both figures that the harmonics with the pure magnitude or frequency-weighted magnitudes are relatively unchanged with different machine loads.

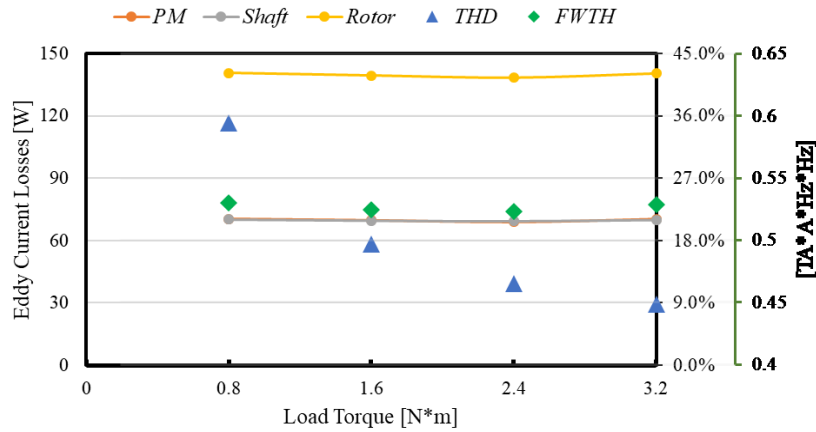


Fig. 13. Rotor losses distribution and THD versus machine load torques.

Fig. 13 shows the PM losses, the shaft losses and the rotor losses against different machine loads obtained from the co-simulation. With a varying load, the rotor losses are nearly unchanged. The calculated current THD and FWTH are also included in Fig. 13. It can be seen from Fig. 13 the current THD drops with a heavier load, which is expected as the fundamental current is more significant. However, FWTH stays relatively stable regardless of load conditions because this indicator only relates to the harmonics instead of the fundamental elements. This trend matches well with the losses versus the machine load conditions.

C. Losses versus Batteries Voltages

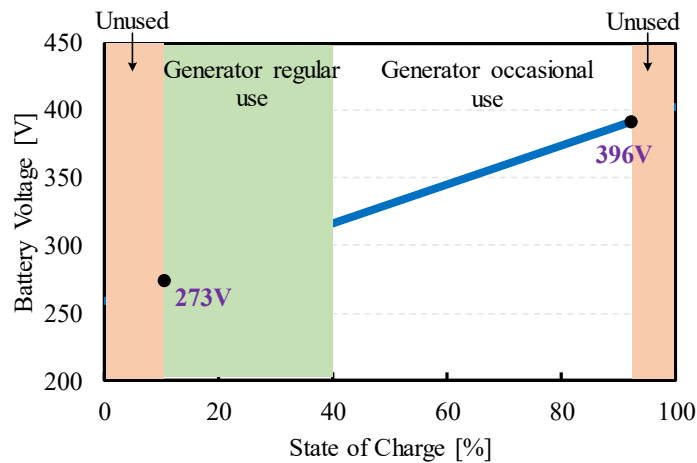


Fig. 14. Delta’s battery pack working profile.

Fig. 14 shows the onboard battery voltage variation against its SoC. This relationship can be assumed linearly when the SoC is between 15% and 95%. Delta Motorsport built this 33kWh battery pack with voltages ranging

from 259V to 403V. It can be seen from Fig. 14 that the generator regular use region is at the battery SoC region of 10% to 40%, and the battery voltage level is regulated between 273V to 395V during driving cycles. Thus, several representative voltage levels within that range are chosen to study the eddy current losses versus battery voltages.

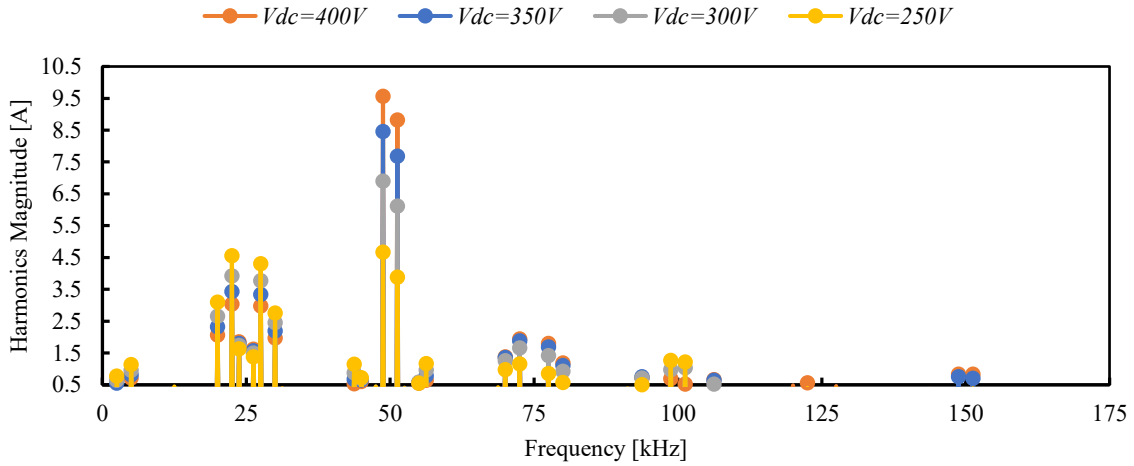


Fig. 15. Magnitudes of current harmonics spectrum using different battery voltages.

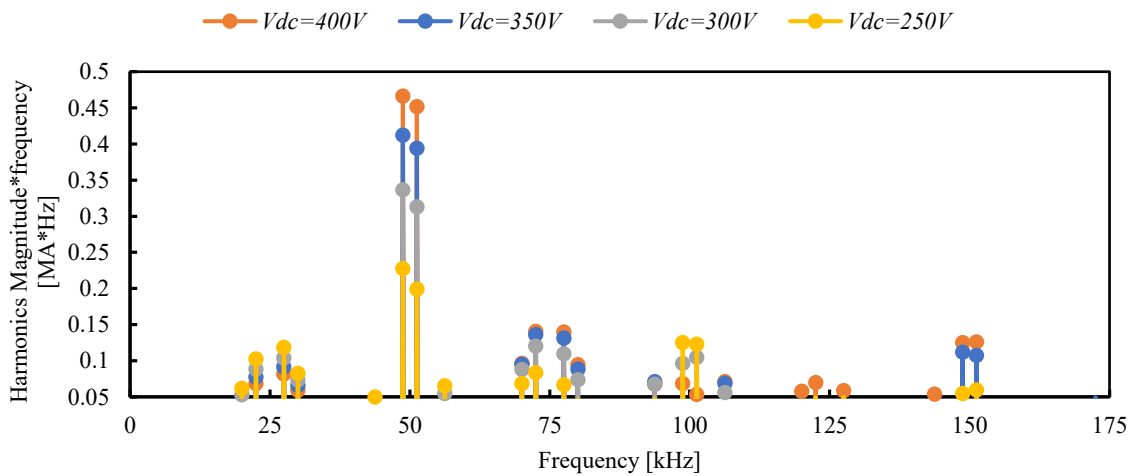


Fig. 16. Frequency-weighted magnitudes of current harmonics spectrum with different battery voltages.

In this study, the switching frequency is maintained at 25kHz, and the machine speed is 75krpm applied with a load torque of 3.2Nm. Fig. 15 shows the magnitudes of current harmonics using the DC-link voltages from 250V to 400V. The current harmonic magnitudes are multiplied by their frequencies in Fig. 16. Fig. 15 shows that the major harmonics are allocated at the sidebands of 1<sup>st</sup> and 2<sup>nd</sup> switching frequencies. The harmonics move from 2<sup>nd</sup>  $f_{sw}$  sidebands to 1<sup>st</sup> sidebands with a lower DC-link voltage, as shown in Fig. 15. For instance, the magnitudes of current harmonics in the 2<sup>nd</sup>  $f_{sw}$  sidebands increase with the DC-link voltage. Conversely, the magnitudes of

current harmonics in the 1<sup>st</sup>  $f_{sw}$  sidebands decrease with the DC-link voltage. Once the magnitudes are frequency-weighted in Fig. 16, prominent harmonics are allocated at sidebands of 2<sup>nd</sup>  $f_{sw}$ .

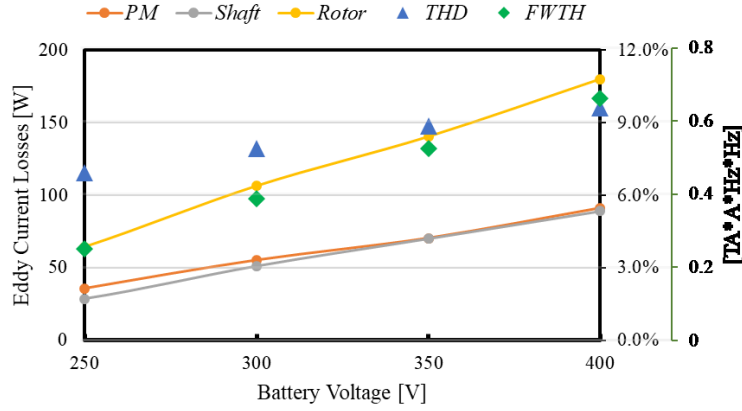


Fig. 17. Rotor losses distribution and FWTH versus DC-link voltages.

Fig. 17 shows the rotor losses distribution, THD and FWTH at different DC-link voltages. The rotor losses comprising the PM losses and the shaft losses increase with a higher DC-link voltage. This finding is expected as the sidebands harmonics around the 2<sup>nd</sup> switching frequencies are dominant ones. Meanwhile, their magnitudes are more significant with a greater DC-link voltage, as seen in Fig. 16. From Fig. 17, it is evident that both THD and FWTH grow with an increasing DC-link voltage, which perfectly matches the trend of rotor losses versus DC-link voltages.

#### D. FWTH Correlation Study

In this paper, the Pearson correlation coefficient (PCC)  $r$  is adopted to access the correlating relationship. This coefficient is widely recognized as a popular method measuring the linear correlation between two sets of data, where its equation is given in (10).

$$r = \frac{\sum (x_i - \bar{x})(y_i - \bar{y})}{\sqrt{\sum (x_i - \bar{x}) \sum (y_i - \bar{y})}} \quad (10)$$

Where  $x_i$  are the values of  $x$ -variable in a sample,  $\bar{x}$  is the mean of the values of the  $x$ -variable,  $y_i$  are values of the  $y$ -variable in a sample, and  $\bar{y}$  is the mean of the values of the  $y$ -variable.

As shown in (10), the PCC is the covariance of two variables dividing by the product of their standard deviations. Therefore, it is essentially a normalized measurement where the result is varying between -1 and 1. A higher absolute value of  $r$  indicates a stronger linear correlation between the chosen two sets of data.

Table II CORRELATIONS BETWEEN THE EDDY CURRENT LOSSES AND THD/FWTH.

Operation Conditions	Different Machine Speeds			Different Machine Loads			Different Batteries		
							Voltages		
Correlations coefficient $r$	Rotor losses	PM losses	Shaft losses	Rotor losses	PM losses	Shaft losses	Rotor losses	PM losses	Shaft losses
THD	0.72	0.45	0.81	0.51	0.46	0.58	1.00	0.99	1.00
FWTH	<b>0.97</b>	<b>0.83</b>	<b>0.99</b>	<b>0.95</b>	<b>0.92</b>	<b>0.98</b>	<b>1.00</b>	<b>1.00</b>	<b>1.00</b>

In Table II, the correlation coefficients between the losses and THD and between the losses and FWTH are calculated under three considered vehicle driving conditions. Table II shows that the correlation coefficients between the rotor eddy current losses and FWTH are greater than 0.95, proving that these two factors are strongly correlated. In comparison, the correlation between the eddy current losses and the THD is relatively weak. Taking the different machine speeds as an example, the value of  $r$  between the rotor losses and THD is only 0.72, as recorded in Table II. In summary, Table II can demonstrate that FWTH is a more suitable indicator than THD in correlating with the eddy current losses.

## VI. EXPERIMENT VALIDATIONS

To validate the direct correlation between the proposed FWTH factor and eddy current losses as seen in the co-simulation, experimental results on the 35kW PM machine (with its parameters shown in TABLE I) are provided in this section.

### A. Rig Set-up

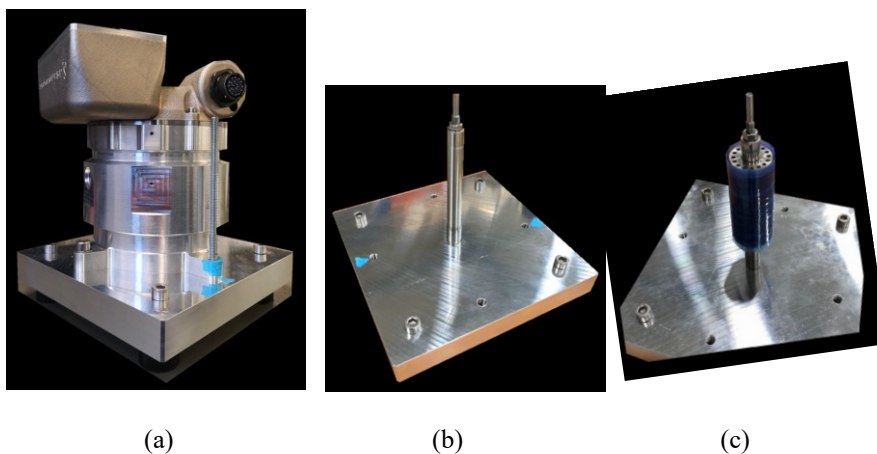


Fig. 18. Locked-rotor rig: a) stator; b) shaft; c) shaft with PM.

To precisely measure the rotor eddy current losses and segregate the PM and shaft losses, a dedicated locked-rotor test rig was employed, as shown in Fig. 18. The shaft in Fig. 18b or Fig. 18c is retained with a stainless M6 nut and plain washer, tightening up to 5Nm. This high stiffness ensures that the rotor will not move even at the rated current since the maximum torque is 3.2Nm, as mentioned in TABLE I. Although the PM in Fig. 18c is demagnetized, some magnetic force may generate due to the remnant magnetization. Compared to the rotational rotor test, the locked one is preferred because the influences of the air friction losses, bearing losses, mechanical losses etc., are removed. Such rig enables segregating the eddy current losses on the PM and the shaft from the stator.

The loss segregation is achieved by measuring the losses under three different set-ups: 1) Since the machine rotor is removable, the stator loss is the loss when there is no rotor installed, as shown in Fig. 18a. 2) When the additional pure shaft in Fig. 18b is assembled with the stator, the loss measured is considered as the sum of the stator loss and shaft loss. 3) Lastly, when the rotor comprising the shaft and the PM in Fig. 18c is mounted, the loss is the sum of the stator loss, the shaft loss, and the PM loss. With all the above three losses from different set-ups, the shaft losses and the PM losses can be properly segregated.

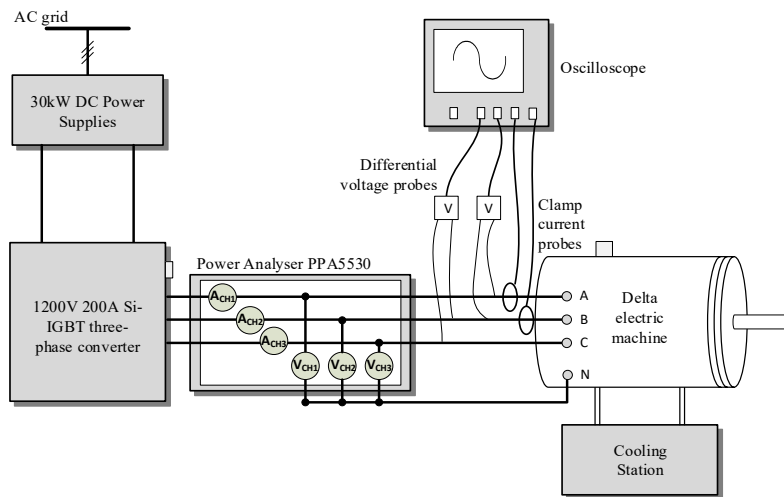


Fig. 19. Experimental rig configuration.

Fig. 19 shows the configuration of the rig under test. The power analyser is employed to measure the losses according to three-terminal phase voltages, phase currents, and their phase shifts. The loss is considered as the active power flowing from the converter to the Delta machine in Fig. 19. Besides, the power analyser takes the fundamental losses into account by calculating the active power using the fundamental components in currents

and terminal voltages. Hence, the fundamental loss must be subtracted for obtaining the eddy current losses solely due to time harmonics.

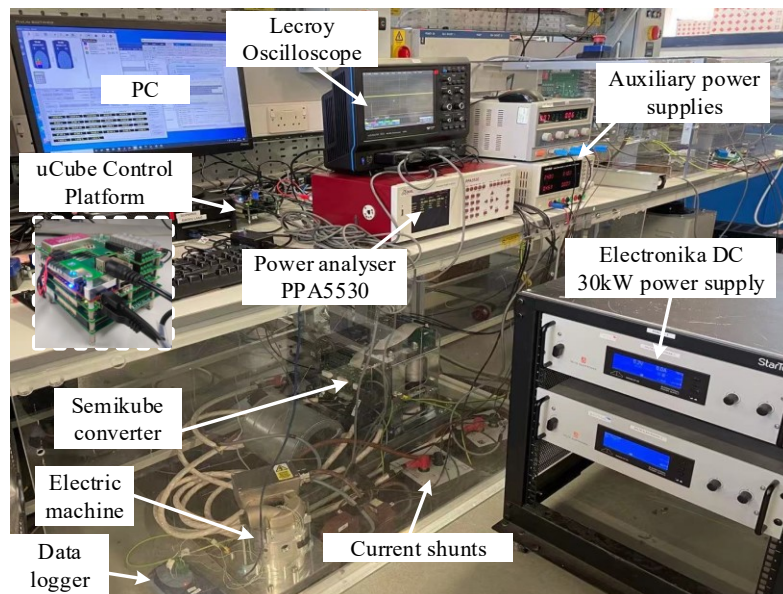
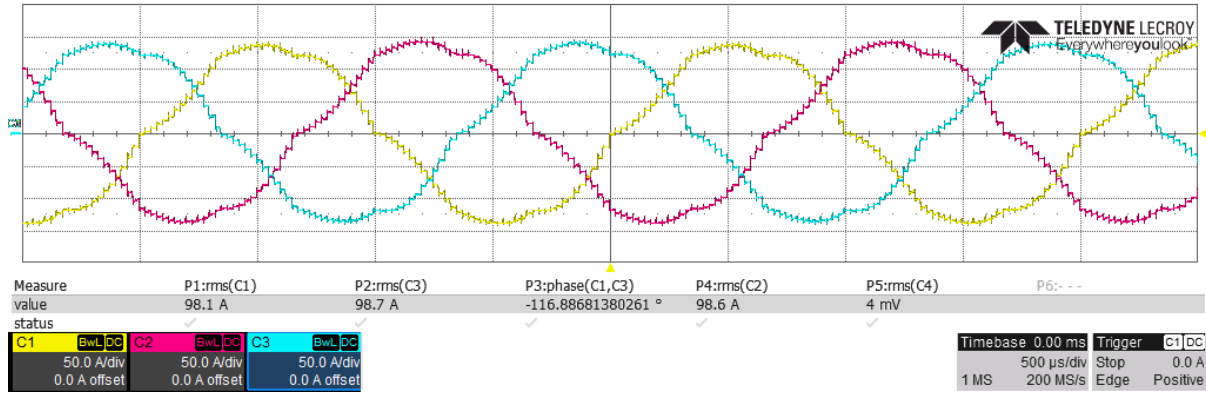


Fig. 20. Experimental rig set-up.

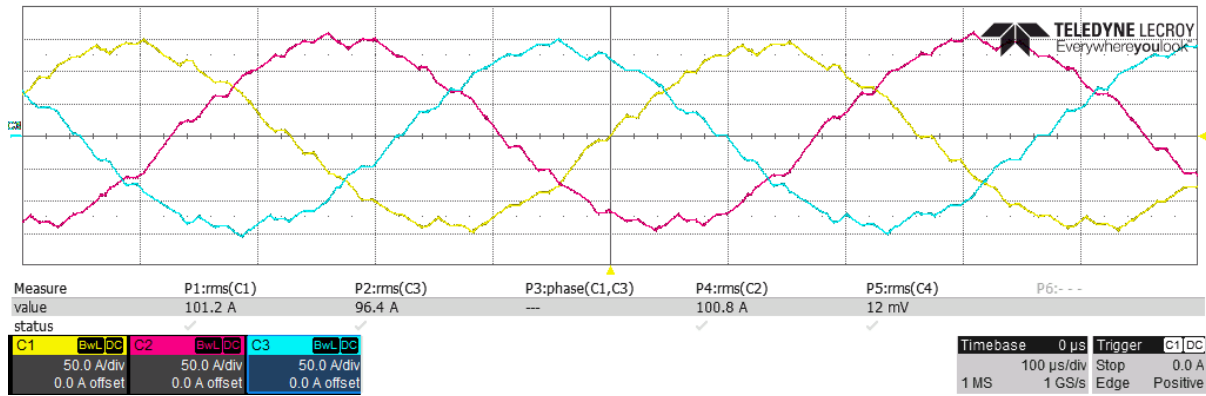
The experimental rig is shown in Fig. 20. The PPA5530 is chosen as the power analyzer, providing exceptional measurement stability and a phase angle accuracy of 0.005 degrees. The current shunts in Fig. 20 are the dedicated devices that can enhance the current measurement capability of the PPA5530 up to 200A. As shown in Fig. 20, a 30kW DC power supply feeds the power into the converter. The employed Semikube converter from Semikron is an air-cooled three-phase IGBT stack rating at 1200V and 200A, which is controlled by a high-performance control platform called uCube [27]. The phase currents and voltages waveforms are captured using the Lecroy oscilloscope. To prevent the potential damage to the PM from overheat, the machine temperature is monitored during the tests. There are three K-type thermal couplers placed at the middle of stator slots, while the data logger interprets the temperature and send this information to the PC for display.

### B. Results with Different Machine Speeds

This part contains the eddy current losses results with different machine speeds varying from 10krpm to the full speed of 110krpm. Those speeds correspond to the fundamental frequency ranging from 167Hz to 1833Hz. All the tests are carried out under the same rated current of 145A and the same switching frequency of 20kHz. The three-phase currents waveforms of two representative cases with 30krpm and 110krpm are shown in Fig. 21. It can be seen that the currents under 30krpm in Fig. 21a are more distorted than under 110krpm in Fig. 21b.



(a)



(b)

Fig. 21. Experimental results of three-phase currents with machine speeds of a) 30krpm (500Hz); b) 110krpm (1833Hz).

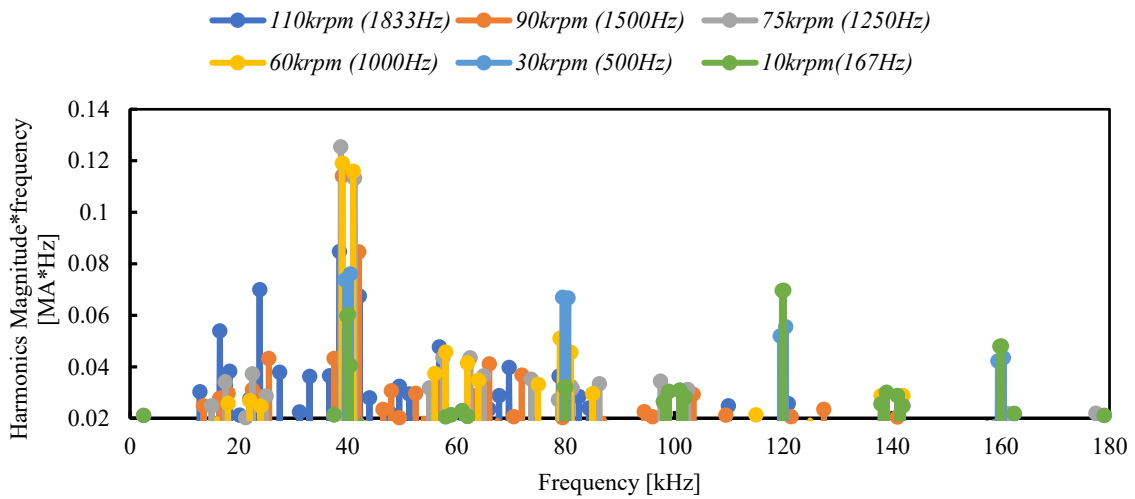


Fig. 22. Experimental results of frequency-weighted magnitudes of current harmonics with different machine speeds.

Fig. 22 shows the frequency-weighted magnitudes of current harmonics at six tested machine speeds, i.e., 10krpm, 30krpm, 60krpm, 75krpm, 90krpm, and 110krpm. Similar to the findings in simulations, the sidebands of 2<sup>nd</sup>

switching frequencies are still dominant, as shown in Fig. 22. In particular, the harmonics with 60krpm in yellow colour and 75krpm in grey colour have the highest frequency-weighted harmonics in that sideband.

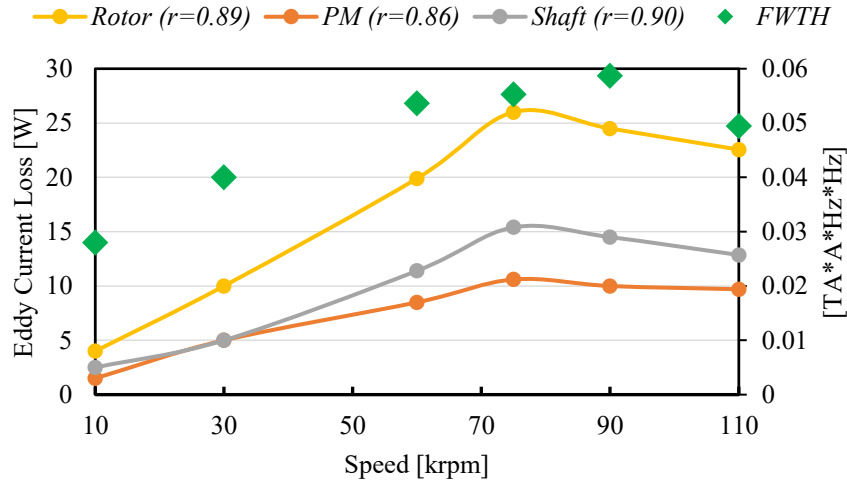


Fig. 23. Experimental results of rotor losses distribution and FWTH factors versus machine speeds.

Fig. 23 shows the rotor losses segregation between the PM and the shaft versus different machine speeds. A similar trend can be observed with the simulation results in Fig. 10. The eddy current losses will initially increase with the speeds and then drop at full speed. Besides, the FWTHs with different speeds are computed and added to the secondary vertical axis of Fig. 23. To evaluate the correlation between the FWTH and the eddy current losses, the PCC factors  $r$  are included in the legends of Fig. 23. For instance, the PCC between the FWTH and the rotor losses is  $r = 0.89$ , which is a considerably strong correlation. The experimental results showed in Fig. 23 validate that the FWTH factor can well indicate the eddy current losses variations against machine speeds.

### C. Results with Different Machine Loads

The eddy current losses with different loads varying from a quarter load to rated load are studied in this part. Due to the locked rotor, the varying loads are emulated by injecting their corresponding current values. Apart from the load, the machine is maintained at the rated speed, and the switching frequency is 20 kHz. Fig. 24 shows the frequency-weighted magnitudes of current harmonics versus different loads. This spectrum is different from the simulated one in Fig. 12, where the frequency-weighted harmonics are unchanged regardless of the changing loads. In contrast, the experimental results in Fig. 24 show that the harmonics are increasing with the load torques. This disagreement results from the fact that no actual load torque can be applied with the demagnetized lock-rotor rig. In consequence, the power factor is always low regardless of increasing currents. However, in a back-to-back rotational rig, the power factor climbs up with greater load torques. When the same stator voltage applies to the

rotational and locked rotor rig, the phase currents harmonics will be distinct as the power factors are different in these two cases.

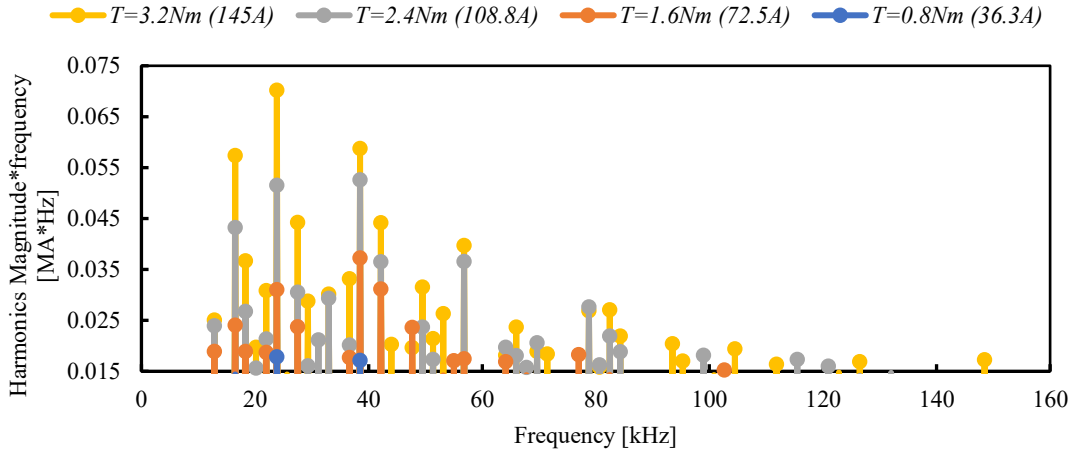


Fig. 24. Experimental results of frequency-weighted magnitudes of current harmonics with different machine loads.

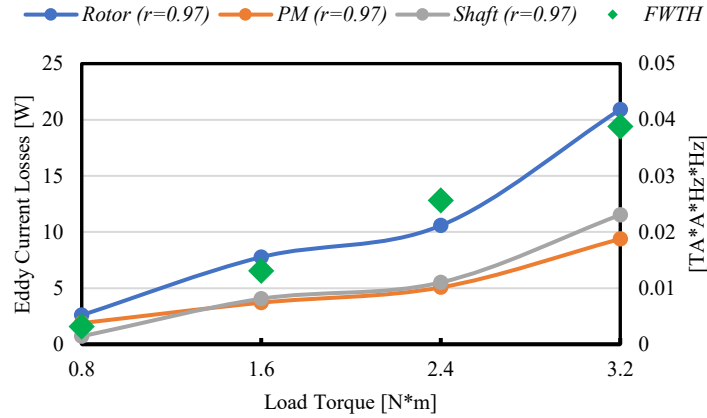


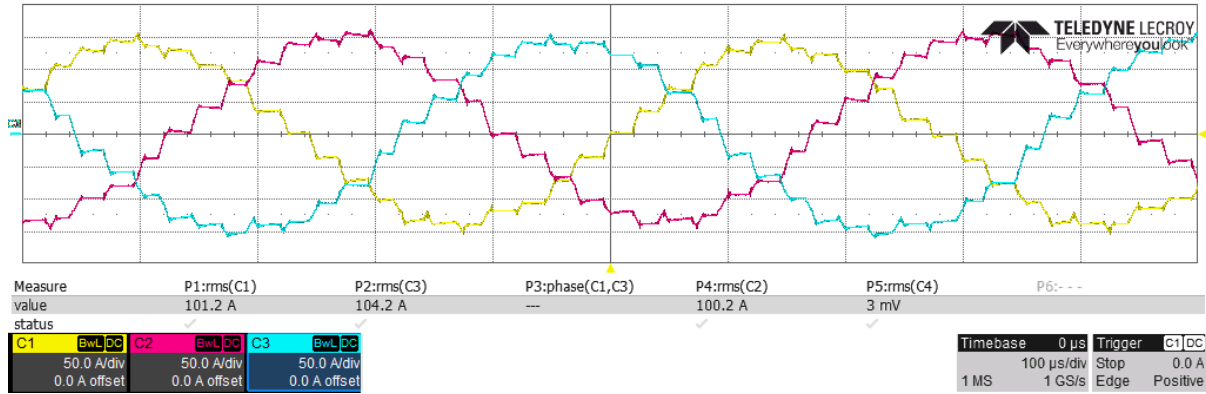
Fig. 25. Experimental results of rotor losses distribution and FWTH factors versus machine loads.

The experimental result of rotor losses with varying loads is shown in Fig. 25. It is apparent that all the losses are increasing with a larger torque due to the increased current harmonics in Fig. 24. As explained in the previous paragraph, the test condition is different from the simulation. However, Fig. 25 shows that despite the discrepancy between the simulation and experimental tests, FWTHs are still correlated to the rotor loss well with  $r = 0.97$ .

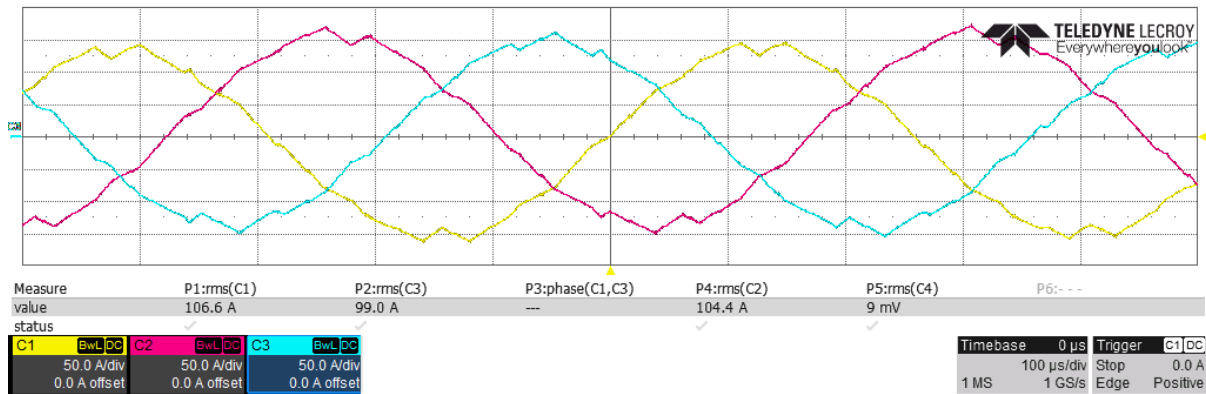
*D. Results with Different Battery Voltages*

This part contains the eddy current losses results with different battery voltages. This varying voltage is achievable by adjusting the DC-link voltage. All the tests use the same speed of 110krpm, same rated current of 145A and the same switching frequency of 20kHz. The three-phase currents waveforms of two representative cases with

120V and 300V are shown in Fig. 26. It can be seen from Fig. 26 that the currents with 300V DC-link voltage in Fig. 26a are more distorted than the ones with 120V DC-link voltage in Fig. 26b. This observation is verified in the frequency-weighted harmonics showed in Fig. 27.



(a)



(b)

Fig. 26. Experimental results of three-phase currents with DC-link voltages of a) 300V; b) 120V.

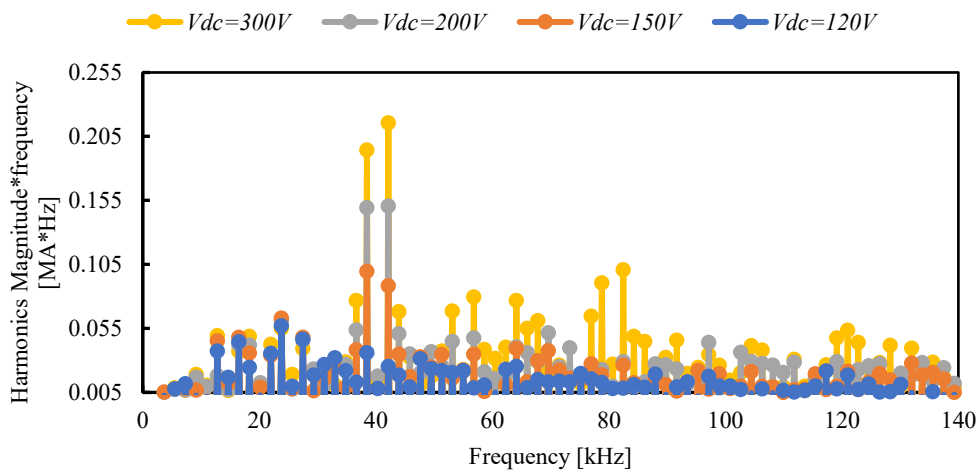


Fig. 27. Experimental results of Frequency-weighted magnitudes of current harmonics with different DC-link voltages.

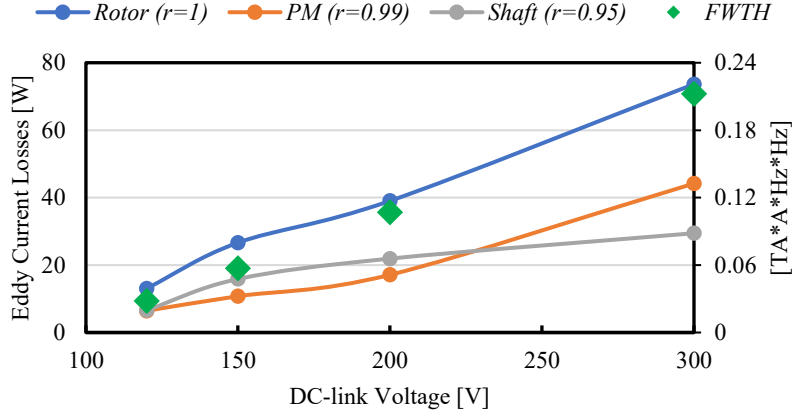


Fig. 28. Experimental results of rotor losses distribution and FWTH factors versus DC-link voltages.

Finally, the experimental result of rotor losses with varying DC-link voltage is shown in Fig. 28. It is obvious that all the losses are increasing with a higher DC-link voltage. This finding agrees with the outcomes seen in simulation results (see Fig. 17). Besides, Fig. 28 also shows that the PCC between the FWTH and the rotor loss is  $r = 1$ . The experimental results in Fig. 28 can validate that the FWTH factor can indicate well the eddy current losses variations versus DC-link voltages.

Table III EXPERIMENTAL CORRELATIONS BETWEEN THE EDDY CURRENT LOSSES AND THD/FWTH.

Operation Conditions	Different Machine Speeds			Different Machine Loads			Different Batteries Voltages		
	Rotor losses	PM losses	Shaft losses	Rotor losses	PM losses	Shaft losses	Rotor losses	PM losses	Shaft losses
Correlations coefficient $r$									
THD	0.54	0.25	0.61	0.43	0.41	0.43	0.80	0.88	0.60
FWTH	<b>0.89</b>	<b>0.86</b>	<b>0.90</b>	<b>0.97</b>	<b>0.97</b>	<b>0.97</b>	<b>1.00</b>	<b>0.99</b>	<b>0.95</b>

Table III records the correlation coefficients between the losses and FWTH/THD in the experimental results concerning different vehicle driving conditions. It is apparent from Table III that a strong correlation between the rotor eddy current losses and FWTH is demonstrated by at least  $r = 0.89$ . In comparison, the correlation between the eddy current losses and the THD is relatively weak. Taking the different machine speeds as an example, the PCC between the rotor losses and THD is only 0.54, as seen in Table III. From above all, Table III can prove that FWTH is a more suitable indicator than THD in correlating with the eddy current losses.

## VII. DISCUSSIONS

Through the FEA results in Section V and the experimental results in Section VI, a strong correlation between the addressed FWTH factor and the eddy current losses has been well validated. For estimating the rotor losses, previously addressed methods are either running the time-consuming 3D FEA (one single case takes more than one day, as discussed in Section IV. B) [15] or solving complex analytical equations [11, 14, 16, 17]. In contrast, deriving the FWTH indicators takes seconds because they are calculated by simply governing all the current harmonics, as expressed in (5). Besides, the machine and converter operation conditions considered in this paper, covering the machine speeds and loads and converter DC-link voltages, significantly affect the current harmonics distribution. However, those variables have not been adequately investigated in the previous works. For example, only the losses variations at different DC-link voltages were examined in [17].

Using FWTH can be considerably helpful for fast characterizing the rotor losses of the machines. After calculating FWTHs at different machine and converter operation conditions, the one associated with the greatest rotor eddy current losses can be identified. This operation point can assist the preliminary design of the drive system and the design of the thermal management system. Further, any potential rotor losses optimization methods can be tested by comparing their associated FWTHs. This indicator can be particularly beneficial for the machines in PHEV applications where the rotor losses usually are excessive due to high-speed operation. Taking the chosen 110krpm PM machine served in PHEV as an example, using FWTHs can quickly identify that the worst eddy current losses will occur at medium speeds with the highest applicable battery voltage. The rotor losses management and optimization methods should focus on that case.

## VIII. CONCLUSIONS

In this paper, an indicator called FWTH was defined to correlate with the eddy current losses of high-speed PM machines. The eddy current losses at variable machine operation conditions of speeds and loads and variable converter operation conditions of battery voltages have been comprehensively studied in this paper. Both co-simulation results and the experimental results on a commercial 35kW, 110krpm PM machine have validated the strong correlation between the FWTH and the eddy current losses. It has been found that the chosen high-speed machine will experience the worst eddy current losses at medium speeds with the highest applicable battery voltage. This operation point should be taken as the case for future eddy current losses reduction studies.

## REFERENCES

- [1] I. Aghabali, J. Bauman, P. Kollmeyer, Y. Wang, B. Bilgin, and A. Emadi, "800V Electric Vehicle Powertrains: Review and Analysis of Benefits, Challenges, and Future Trends," *IEEE Transactions on Transportation Electrification*, 2020.
- [2] R. T. Mehrjardi, N. F. Ershad, and M. Ehsani, "Transmotor-Based Powertrain for High-Performance Electric Vehicle," *IEEE Transactions on Transportation Electrification*, vol. 6, no. 3, pp. 1199-1210, 2020.
- [3] M. Ehsani, K. V. Singh, H. O. Bansal, and R. T. Mehrjardi, "State of the Art and Trends in Electric and Hybrid Electric Vehicles," *Proceedings of the IEEE*, 2021.
- [4] C. Liu, K. Chau, C. H. Lee, and Z. Song, "A critical review of advanced electric machines and control strategies for electric vehicles," *Proceedings of the IEEE*, 2020.
- [5] H. Fathabadi, "Plug-in hybrid electric vehicles: Replacing internal combustion engine with clean and renewable energy based auxiliary power sources," *IEEE Transactions on Power Electronics*, vol. 33, no. 11, pp. 9611-9618, 2018.
- [6] H. Zhang, J. Peng, H. Tan, H. Dong, and F. Ding, "A Deep Reinforcement Learning Based Energy Management Framework with Lagrangian Relaxation for Plug-in Hybrid Electric Vehicle," *IEEE Transactions on Transportation Electrification*, 2020.
- [7] W. Wang, X. Chen, and J. Wang, "Motor/generator applications in electrified vehicle chassis—A survey," *IEEE Transactions on Transportation Electrification*, vol. 5, no. 3, pp. 584-601, 2019.
- [8] H. Tu, H. Feng, S. Srdic, and S. Lukic, "Extreme fast charging of electric vehicles: A technology overview," *IEEE Transactions on Transportation Electrification*, vol. 5, no. 4, pp. 861-878, 2019.
- [9] S. Li, Y. Li, W. Choi, and B. Sarlioglu, "High-speed electric machines: Challenges and design considerations," *IEEE Transactions on Transportation Electrification*, vol. 2, no. 1, pp. 2-13, 2016.
- [10] N. Schofield and S. Long, "Generator operation of a switched reluctance starter/generator at extended speeds," *IEEE transactions on vehicular technology*, vol. 58, no. 1, pp. 48-56, 2008.
- [11] S. Jumayev, M. Merdzan, K. Boynov, J. Paulides, J. Pyrhönen, and E. Lomonova, "The effect of PWM on rotor eddy-current losses in high-speed permanent magnet machines," *IEEE transactions on magnetics*, vol. 51, no. 11, pp. 1-4, 2015.
- [12] J. Ma and Z. Zhu, "Magnet eddy current loss reduction in permanent magnet machines," *IEEE Transactions on Industry Applications*, vol. 55, no. 2, pp. 1309-1320, 2018.

- [13] N. Chiodetto, N. Bianchi, and L. Alberti, "Improved analytical estimation of rotor losses in high-speed surface-mounted PM synchronous machines," *IEEE Transactions on Industry Applications*, vol. 53, no. 4, pp. 3548-3556, 2017.
- [14] M. Cheng and S. Zhu, "Calculation of PM eddy current loss in IPM machine under PWM VSI supply with combined 2-D FE and analytical method," *IEEE Transactions on Magnetics*, vol. 53, no. 1, pp. 1-12, 2016.
- [15] J.-X. Shen and X.-F. Qin, "Investigation of Rotor Eddy Current Loss in High-Speed PM Synchronous Motor with Various PWM Strategies," in *2020 Fifteenth International Conference on Ecological Vehicles and Renewable Energies (EVER)*, 2020: IEEE, pp. 1-5.
- [16] S. Zhu, W. Hua, and B. Shi, "Comparison of Methods Using Different Sources for Computing PWM Effects on Permanent Magnet Machines Considering Eddy Current Reaction," *IEEE Transactions on Magnetics*, vol. 57, no. 6, pp. 1-4, 2021.
- [17] J. Ou, Y. Liu, D. Liang, and M. Doppelbauer, "Investigation of PM Eddy Current Losses in Surface-Mounted PM Motors Caused by PWM," *IEEE Transactions on Power Electronics*, vol. 34, no. 11, pp. 11253-11263, 2019, doi: 10.1109/TPEL.2019.2895679.
- [18] D. Cao, W. Zhao, T. Liu, and Y. Wang, "Magneto-Electric Coupling Network Model for Reduction of PM Eddy Current Loss in Flux-Switching Permanent Magnet Machine," *IEEE Transactions on Industrial Electronics*, 2021.
- [19] Z. Huang, T. Yang, P. Giangrande, S. Chowdhury, M. Galea, and P. Wheeler, "Enhanced Performance of Dual Inverter With a Floating Capacitor for Motor Drive Applications," *IEEE Transactions on Power Electronics*, vol. 36, no. 6, pp. 6903-6916, 2020.
- [20] Z. Huang, T. Yang, P. Giangrande, S. Chowdhury, M. Galea, and P. Wheeler, "An active modulation scheme to boost voltage utilization of the dual converter with a floating bridge," *IEEE Transactions on Industrial Electronics*, vol. 66, no. 7, pp. 5623-5633, 2018.
- [21] F. Guo, T. Yang, C. Li, S. Bozhko, and P. Wheeler, "Active Modulation Strategy for Capacitor Voltage Balancing of Three-Level Neutral-Point-Clamped Converters in High-Speed Drives," *IEEE Transactions on Industrial Electronics*, 2021.
- [22] P. Pfister, X. Yin, and Y. Fang, "Slotted Permanent-Magnet Machines: General Analytical Model of Magnetic Fields, Torque, Eddy Currents, and Permanent-Magnet Power Losses Including the Diffusion

- Effect," *IEEE Transactions on Magnetics*, vol. 52, no. 5, pp. 1-13, 2016, doi: 10.1109/TMAG.2015.2512528.
- [23] P. Lee, K. Kuo, C. Wu, Z. Wong, and J. Yen, "Prediction of iron losses using the modified Steinmetz equation under the sinusoidal waveform," in *2011 8th Asian Control Conference (ASCC)*, 15-18 May 2011 2011, pp. 579-584.
- [24] H. Matsumori, T. Shimizu, T. Kosaka, and N. Matsui, "Iron loss calculation under PWM inverter switching for SiFe steel materials," in *2019 IEEE Energy Conversion Congress and Exposition (ECCE)*, 29 Sept.-3 Oct. 2019 2019, pp. 2315-2320, doi: 10.1109/ECCE.2019.8912818.
- [25] C. Wang, T. Yang, H. Hussaini, Z. Huang, and S. Bozhko, "Power Quality Improvement Using an Active Power Sharing Scheme in More Electric Aircraft," *IEEE Transactions on Industrial Electronics*, 2021.
- [26] A. Demenko, R. M. Wojciechowski, and J. K. Sykulski, "2-D versus 3-D electromagnetic field modeling in electromechanical energy converters," *IEEE transactions on magnetics*, vol. 50, no. 2, pp. 897-900, 2014.
- [27] A. Galassini, G. L. Calzo, A. Formentini, C. Gerada, P. Zanchetta, and A. Costabeber, "uCube: Control platform for power electronics," in *2017 IEEE Workshop on Electrical Machines Design, Control and Diagnosis (WEMDCD)*, 2017: IEEE, pp. 216-221.